Volume 18 | Number 7 | 7 April 2016 | Pages 1821–2242

Green Chemistry

Cutting-edge research for a greener sustainable future
www.rsc.org/greenchem

ISSN 1463-9262

ROYAL SOCIETY OF CHEMISTRY

CRITICAL REVIEW
G. Chatel et al.
Heterogeneous catalytic oxidation for lignin valorization into valuable chemicals: what results? What limitations? What trends?

175 YEARS

This is an Accepted Manuscript, which has been through the Royal Society of Chemistry peer review process and has been accepted for publication.

Accepted Manuscripts are published online shortly after acceptance, before technical editing, formatting and proof reading. Using this free service, authors can make their results available to the community, in citable form, before we publish the edited article. We will replace this Accepted Manuscript with the edited and formatted Advance Article as soon as it is available.

You can find more information about Accepted Manuscripts in the author guidelines.

Please note that technical editing may introduce minor changes to the text and/or graphics, which may alter content. The journal's standard Terms & Conditions and the ethical guidelines, outlined in our author and reviewer resource centre, still apply. In no event shall the Royal Society of Chemistry be held responsible for any errors or omissions in this Accepted Manuscript or any consequences arising from the use of any information it contains.

ROYAL SOCIETY OF CHEMISTRY

rsc.li/green-chem

Microplasma-assisted electrochemical synthesis of Co₃O₄ nanoparticles in absolute ethanol for energy applications[†]

Chengsheng Ni[a,b,c]*, Darragh Carolan[a], Conor Rocks[a], Jianing Hui[b], Zeguo Fang[b], Dilli Babu Padmanaban[a], Jiupai Ni[c], Deti Xie[c], Paul Maguire[a], John T.S. Irvine[b] and Davide Mariotti[a]

a. School of Engineering, University of Ulster, Jordanstown campus, Shore Road, Newtownabbey, Northern Ireland, UK, BT37 0QB.

b. School of Chemistry, University of St Andrews, St Andrews, UK, Scotland, KY16 9ST

c. College of Resources and Environment, Southwest University, Beibei, Chongqing, 400716, China

*Corresponding author: C.N.: nichengsheg@swu.edu.cn; nichengsheg@gmail.com;

† Electronic Supplementary Information (ESI) available: [Valence band XPS, testing set-up, SEM and et al.]. See DOI: 10.1039/x0xx00000x

Plasma at the gas/liquid interface can promote a complex mixture of reactions in solution and microplasma-assisted direct-current anodic oxidation is an efficient and green process in synthesising nanoscale materials for various applications. In this study, we demonstrated the direct synthesis of crystalline Co₃O₄ quantum dots, *ca.* 2-5 nm in diameter, by direct anodization of Co foil with charge balanced by the microplasma at the flowing-helium/pure-ethanol interface under ambient condition. The anodic oxidation of cobalt in ethanol was analysed after characterising the solution using nuclear magnetic resonance (NMR), light absorption, photoluminescence (PL), and the solid product using X-ray photoemission spectroscopy (XPS), X-ray diffraction (XRD), and thermogravimetric analysis (TGA). In the microplasma process, at high applied voltage, ethanol was oxidised to acetate

T

acting as the charge carrier and the size of Co_3O_4 quantum dots could be controlled by the limiting current. The quantum dots from this method are well dispersed in ethanol and a dense coating for light absorption and a rectified diode can be processed directly from the suspension. These results reveal that microplasma-assisted anodisation in ethanol is an efficient and green route capable of manufacturing quantum dots at low-temperature and avoiding the use of extraneous ionic salts in electrolyte.

Introduction

Crystalline nanoparticles are recognised to exhibit unique size effects with important consequences on their electronic structure, mass transfer and interface, which are key aspects to develop novel industrial applications[1-3]. Nanocrystalline cobalt-oxide spinels have been extensively explored for many energy conversion and storage technologies, including batteries, fuel cells, electrolysers and solar cells[4-9]. The synthesis of Co_3O_4 spinel has been achieved by thermal decomposition of cobalt nitrate at 400 ^{o}C with nanoparticles sizes close to 50 nm.[10] Electrochemical deposition of a Co_3O_4 coating was carried out on fluorine-doped tin oxide via pulsed cathodic/anodic current from a $CoCl_2$ solution, followed by thermal treatment at 500 ^{o}C.[11] Jing *et al.*[12] synthesized $Co(OH)_2/Co_3O_4$ by anodising two Co electrodes in aqueous NaCl solution under an alternate-current at 8 V. Chu *et al.*[8] synthesized a cobalt oxide dispersion (*ca.* 10 nm) directly using a glow–discharge plasma in an aqueous cobalt nitrate solution following a typical Fischer–Tropsch synthesis. Co_3O_4 quantum dots under 10 nm in diameter have been synthesised using a microwave-assisted solvothermal process and subsequently used for water splitting under visible light where the elevation of the conduction band minimum due to quantum confinement was observed to be beneficial.[13] Co_3O_4 nanocrystals smaller than 5 nm in diameter have been deposited in-situ on $CaMn_4O_5$ from

pentaamminecobalt (III) chloride, which was oxidized under visible light during the photocatalytic process[14].

Plasmas confined within a sub-millimetre gap are generally referred to as *microplasmas*[15]. In recent years, microplasma-assisted electrochemical synthesis in aqueous electrolytes has been utilised to produce a wide range of nanomaterials including quantum dots made of nitrogen-doped carbon,[16, 17] gold[18-20], platinum[21], cupreous oxide[22-24] or zinc sulphide[25]. The introduction of a gaseous-plasma electrode at the liquid/gas interface provides new pathways for electrochemical reactions because of the non-Faradaic processes; ultraviolet radiation, ions and electrons from the plasma can act simultaneously together with charge transfer and lead to unprecedented reaction products.[26] Non-Faradaic reactions are expected to change the intermediate species involved in the electrochemical process and for instance the addition of around 8 vol. % ethanol into the aqueous electrolyte has been observed to affect the amount of hydroxyl radicals and accelerate the production of Au quantum dots by microplasma synthesis.[27, 28] Liquid ethanol, an important media as the dispersant for quantum dots, is reported to tolerate high electron density ($\approx 10^{19}$ m^{-3}) under direct-current (DC) plasma inducing highly non-equilibrium kinetically driven reactions that would not be achievable in standard electrochemistry or by radiolysis techniques.[29, 30] For example, one of the important intermediate products formed from the reaction between silicon and alcohol is the Si-OR (R is the alkyl group), which makes the surface reactions of Si in ethanol different from that in water.[30, 31]

In order to promote green synthesis routes, hazardous chemicals, high energy consumption and lengthy processes (including repeated washing and purification steps) should be avoided.[32-35] Well-dispersed crystalline Co_3O_4 quantum dots were synthesised in this study using plasma-assisted anodic oxidation of pure cobalt solid metal in absolute ethanol as the electrolyte. Ionic salts, reducing agents and

surfactants, that are normally used in established solution-based processes, were here all avoided, reducing the cost and environmental impact of manufacturing chemicals. Also, the absence of extraneous by-products and persistent ions (e.g. NO_3^-, Cl^-, SO_4^{2-}) reduces the number of washing/purifications steps and increases the process yield; these are all important aspects to be considered for implementing green processes.[36, 37] Furthermore, because plasma-assisted synthesis does not require energy intensive sintering/firing processes at high-temperature, it is also energy efficient and can be considered all together as a realistic avenue for the green production of crystalline Co_3O_4 quantum dots. Co_3O_4 quantum dots synthesized in this way can find application in heterojunction solar cells or photo-catalysts, which require the crystal size to be around 1-3 nm for thin and compact film deposition.[38] In fact, a compact and uniform film was prepared using our nanocrystals dispersed in ethanol with nearly no thermal treatment. We found that the interaction between ethanol and the plasma could provide the required carboxylate anions as charge carrier and the size of the crystals could be controlled by the limiting current of the plasma system. The cobalt carboxylate-related by-product can be converted into Co_3O_4 spinels by a low temperature thermal treatment (250 ^{o}C). This study provides a new room-temperature route for synthesising nanocrystals to be used as catalysts or for heterojunction solar cells; it also advances our understanding of the chemistry involved in the treatment of organic electrolytes by microplasmas.

Experimental

20 mL absolute ethanol in a cultivation basin was used as the electrolyte, as shown in Figure S1. A graphite rod (5 mm in diameter) and a cobalt foil (0.1 mm in thickness and 30 mm in width) were used as anode, the latter to produce Co_3O_4 quantum dots and the former to investigate further reactions induced at the plasma-ethanol interface. The immersed area of the Co electrode was around 5.32

cm^2. Helium was flown (50 standard cubic centimetres per minute, sccm) through a nickel tube (0.7 mm inner diameter and 1.0 mm outer diameter) which was used as the cathode to sustain the microplasma. The distance between the end of the nickel tube and the surface of the electrolyte was kept constant at 1.5 mm. An initial voltage of 3 kV from a direct-current power source in series with a ballast resistor of 5 kΩ was applied between the anode and cathode for the initiation of the microplasma. The various processes were all carried out for 40 min and the current limit was set to be 4.6 mA or 0.7 mA.

^{1}H nuclear magnetic resonance (NMR) spectra of the solution in CDCl$_3$ after the microplasma-assisted electrolysis were recorded at 300.06 MHz on a Bruker Advance 300 spectrometer. An ultra-violet/visible (UV/VIS) spectrometer (PerkinElmer Lambda 35) equipped with a 150 mm integrating sphere was used for light absorption measurements. Light absorption of 3 mL solutions in a quartz vial were firstly measured in transmission mode and then inside the integrating sphere. Photoluminescence (PL) was measured on an Ocean Optics spectrometer. Transmission electron microscopy (TEM) images and selective area electron diffraction (SAED) patterns were acquired using a high-resolution JEOL JEM-2100F field emission electron microscope and Gatan Dual Vision 600 charge-coupled device (CCD) operating at an accelerating voltage of 200 keV. TEM samples were prepared by depositing a 40 μL aliquot of the microplasma-treated solution onto a holey carbon-coated copper grid (300 mesh, #S147-3, Agar Scientific), which was allowed to evaporate under ambient conditions for 10 hours. 100 μL of the electrolyzed solution was dropped onto a piece of glass and allowed to dry in ambient air for 5 hours, followed by further drying at 80 $^{\circ}$C for 1 hour or 250 $^{\circ}$C for 30 minutes to obtain a uniform coating. Energy-dispersive spectroscopy (EDS) was performed on a spectrometer equipped on the TEM. The coatings were further characterized by scanning electron microscopy (SEM) and X-ray photoemission spectroscopy (XPS).

XPS spectra were recorded on a Kratos Axis Ultra XPS system with a base pressure of 1×10^{-9} mbar using a monochromatic Al K_α X-ray (1486 eV). The current and voltage were 10 mA and 15 kV, respectively. Specific region scans (C 1s, O 1s, N 1s and Co 2p) were performed at a resolution of 0.05 eV and pass energy of 40 eV. Calibration of obtained spectra was performed using the C 1s peak located at 284.5 eV. Data analysis was done with vision processing software package. SEM images were taken on a JEOL 6700F field emission microscope. X-ray diffraction (XRD) of the coatings was measured on a Bruker D8 diffractometer. Fermi level of the coatings on silicon was measured with a Kelvin probe (KPtechnology) in a linear scanning mode and the values were calibrated against a gold reference. Dense TiO_2 layer on In_2O_3-doped tin oxide (ITO) were prepared via the calcination of titanium isopropoxide solution film at 400 ^{o}C for 2 hours[39]; the coating for the diode on the TiO_2 film was prepared by the same drop casting procedures used for deposition on glass. The current collector contact was deposited on the surface via plasma deposition using a Pd target and the area of the effective diode is 4 mm^2. The powdered products from the dried coating were also used for Fourier transform infrared (FTIR) spectroscopy and Thermo-gravimetric analysis (TGA). The FTIR spectroscopy was measured on a Thermoscientific Nicolet iS5 equipped with an attenuated total reflection (ATR) accessory. The powdered products were directly placed on top of the diamond crystal of the ATR accessory and then the measurements were taken. TGA for the powder was measured firstly in flowing air up to 500 ^{o}C on a NETZSCH 49C thermo-gravimeter and then cooled down to room temperature. The product from TGA in air is then reduced flowing 5% H_2 in Ar. The ramp rate for all the TGA was 5.0 ^{o}C min^{-1}.

Results

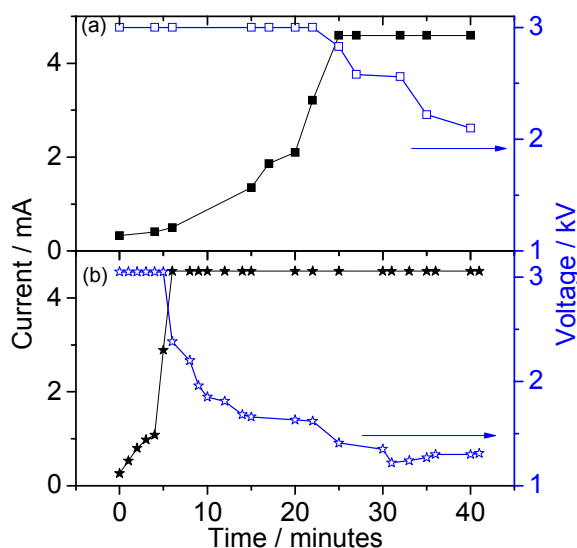**Characterisation of the solution**

Figure 1 Evolution of current and voltage during the experiments with graphite anode (a) and cobalt anode (b) at a limiting current of 4.6 mA.

As pure ethanol shows an acid ionisation constant[40] as low as 10^{-16}, the dissociated cations or anions are in such a small number that the conductivity will limit the initial electrolysis process. The current and voltage evolutions with graphite or cobalt anode are shown in Figure 1. The starting current under 3.0 kV was around 0.2 mA, but the current increased with time until the current set point was reached, indicating that the ionised charge carriers increased during the electrolysis process. The time required for the current to reach 4.6 mA was much shorter when a cobalt anode was used compared to that with a graphite anode, implying that additional charge carriers could possibly be from cobalt-related species. The NMR spectra of pure ethanol and the product after plasma electrolysis with graphite or cobalt anode at 4.6 mA are shown in Figure 2. The NMR spectrum for ethanol contained three major split peaks from the chemical shifts of $-CH_2$, $-CH_3$ and -OH groups, but after the electrolysis with either graphite or cobalt anode, extra minor singlet peaks at 2 ppm from H in the CH_3COO^- group were observed, as shown in Figure 2(b). The peak positions and heights resulting from OH groups were different for the three samples

due to possible differences in the pH or in the sample concentration or in $CDCl_3$. The minor peak shifts of $-CH_2$ and $-CH_3$ for the solution with the graphite anode, 1.168 ppm vs 1.150 ppm for pure ethanol (Figure 2(a)), coupled with the presence of a minor peak for CH_3COO^- are indications of ethyl acetate formation from the condensation of ethanol and acetic acid (AcH).[41] On the other hand, the solution with the Co anode showed no changes in the peak positions for $-CH_3$ and $-CH_2$ groups compared to pure ethanol, indicating that there was no Co ethoxide in the final product. The formation of -OCHO group (δ = 8.0 ppm in Figure 2(c)) after electrolysis indicates that the microplasma process or anodic oxidation can break down the C-C bonds. Since a cobalt anode in aqueous solution was reported to be passivated under an anodic potential of 0.4-1.2 V versus SHE, producing a thin film of CoO/Co_3O_4,[42] the current density of 0.7 mA/cm^2, well above the passivation current (10^{-6} A/cm^2), could be explained by the anodic oxidation of ethanol on the graphite anode or active/trans-passivation dissolution of cobalt oxides. The formation of CH_3COO^- due to the oxidation of ethanol implies that there could be iso-mixed water produced in the electrolysis process along with the absorption of moisture from the ambient air[43], which could affect the oxidation process of cobalt.
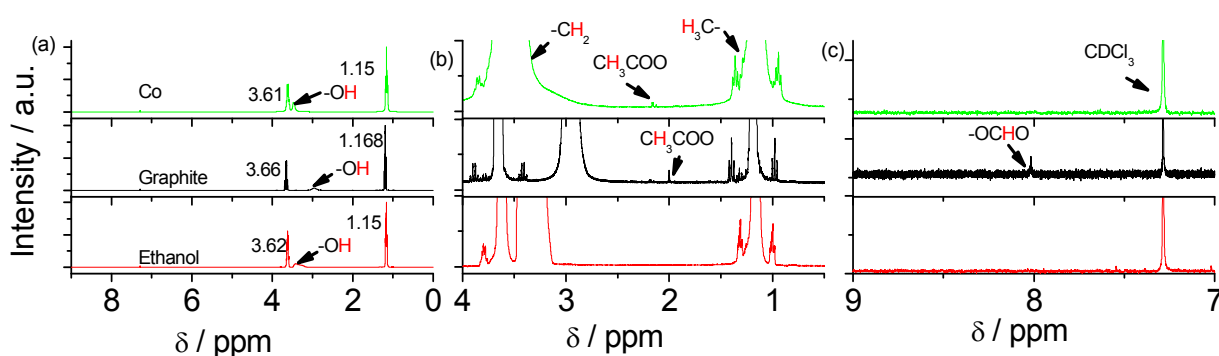

Figure 2. ^{1}H NMR spectra of pure ethanol and solution in $CDCl_3$ after 40 minutes electrolysis at a limiting current of 4.6 mA. Chemical shift of tetramethylsilane (TMS) is calibrated to be zero and the numbers in (a) indicate the central position of the

chemical shifts for proton in -CH_3 and -CH_2. (a), (b) and (c) shows the NMR spectra at different scales.

As Co_3O_4 nanocrystals cannot be detected directly from the proton NMR, the formation of cobalt related species could be inferred from the colouration of the ethanol solution after the electrolysis process. Ultraviolet/visible (UV/Vis) absorption spectra for the undiluted solution and those for solutions diluted ten times and one-hundred times are shown in Figure 3. The Tyndall effect (inset in (b)) was observed for the sample diluted 10 times, proving the formation of a solid suspension. The Tyndall effect, due to light scattering, can be also confirmed from the difference between the absorbance measured in normal transmission mode and the absorbance obtained when the solution was inserted inside integrating sphere; the latter essentially produces a measurement that corresponds to the light from both scattering as well as the transmitted beam. The difference is more pronounced at shorter wavelength due to the higher extent of light scattering from nanocrystals. Moreover, scattering is dependent on the dilution: it is more obvious for the undiluted solution but is indistinguishable for the solution diluted by one-hundred times.
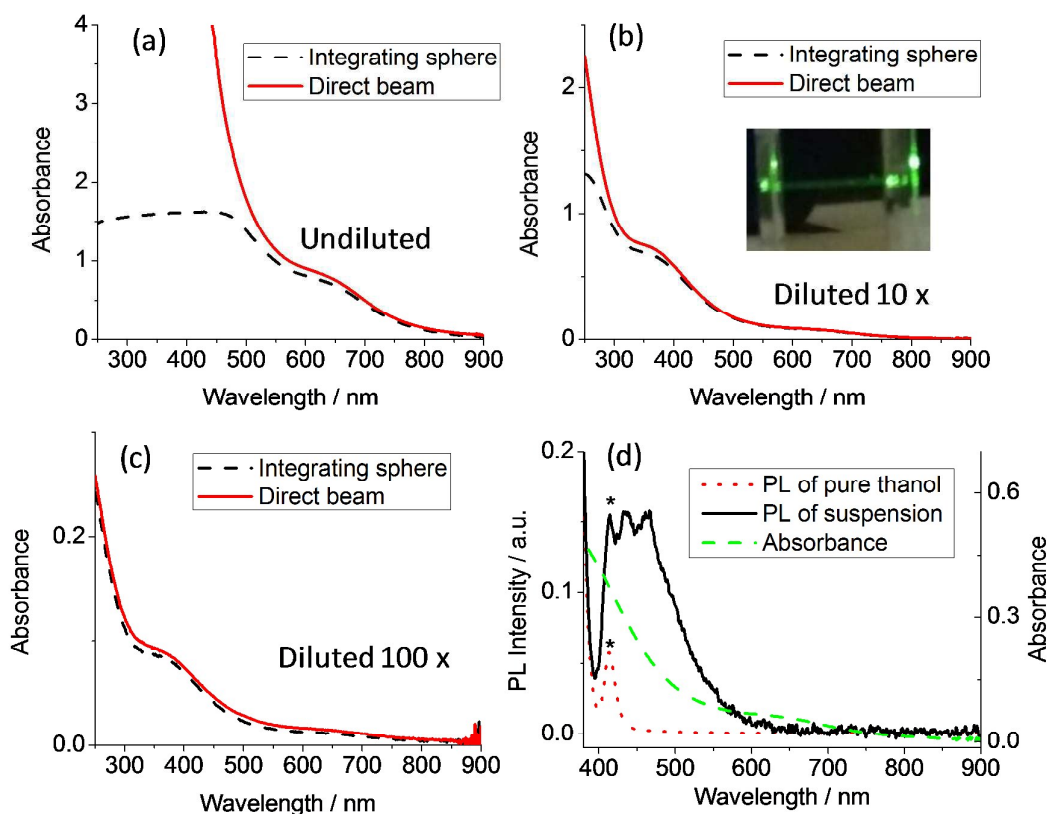
Figure 3 Comparative absorbance of the colloids measured by putting the solution in the middle of a direct beam and inside an integrating sphere. (a), (b) and (c) are the measurements with a dilution coefficient of 1, 10 and 100, respectively. (d) Superimposed photoluminescence (PL) and absorbance of the sample prepared under a limiting current of 4.6 mA with a dilution coefficient of 10. The inset in (b) is a photo showing the Tyndall effect for the suspension diluted by ten times. The * mark in (d) shows the emission peak of ethanol.

The energy gaps of p-type Co_3O_4, which correspond to the edges of the O^{2-}-Co^{3+} excitation and O^{2-}-Co^{2+} charge transfer, were normally reported to be direct transitions at 1.45 eV and 2.07 eV.[44] More recent studies based on absorption, photoluminescence and selective photoexcitation found that additional band transitions in the near-infrared (NIR) region at 0.74 eV or 0.82 eV are also possible (due to the localized d–d transitions of Co^{2+}).[45, 46] However, this absorption tail in the

NIR region is weak and can only be observed when the size of the crystals is larger than 60 nm. The absorbance measured for our solutions shows a peak at 675 nm for the sample synthesized at 4.6 mA, which is blue-shifted with respect to the broad absorption centred around 750 nm of bulk cobalt oxide,[47] and it is a clear indication of quantum confinement.[48] By-products in the final solution such as Co ions and carboxylate anions could also contribute to the absorbance, but the analysis of diluted solutions showed that these by-products had negligible effect for wavelengths above 450 nm as shown in Figure S2. The PL of Co_3O_4 nanoparticles of 5 nm in size has been reported to peak at 560-570 nm,[49] and, as a result, the peak at 430 nm or 460 nm (Figure 3(d)) in the diluted suspension could be attributed to the emission of the by-products. Similarly to other reports for solid [46] and suspended[49] Co_3O_4, no obvious PL emission was observed near the bandgap at 1.5-1.6 eV.

Characterization of solid products

TEM images of the dried samples in air (Figure 4) showed nanocrystals for both samples prepared using 4.6 mA and 0.7 mA limiting current. The sample produced with a current limit of 4.6 mA contained nanocrystals with a mean diameter of about 1.9 nm and the *d*-spacing matches that of the (222) crystal plane of Co_3O_4 with Fd-3m symmetry (Figure 4a-b). The crystals from the sample with 0.7 mA limiting current produced particles with mean diameter of 4.6 nm (Figure 4c). The corresponding size distributions are shown in Figure S3. EDS data (Figure S4) confirms the existence of Co in the dried product. The detailed *d*-spacings on the sample with 0.7 mA limiting current are plotted in Figure 4(e); the SAED diffraction pattern shows perfect diffraction rings for poly-crystalline spinel oxide Co_3O_4. XRD analysis (Figure S5) of the coating dried at 80 °C did not show peaks corresponding to Co_3O_4 crystals; however, after low-temperature calcination at 250 °C, wide peaks corresponding to the spinel

phase could be identified. The absence of peaks in the dried sample could be related to the small size of the quantum dots.
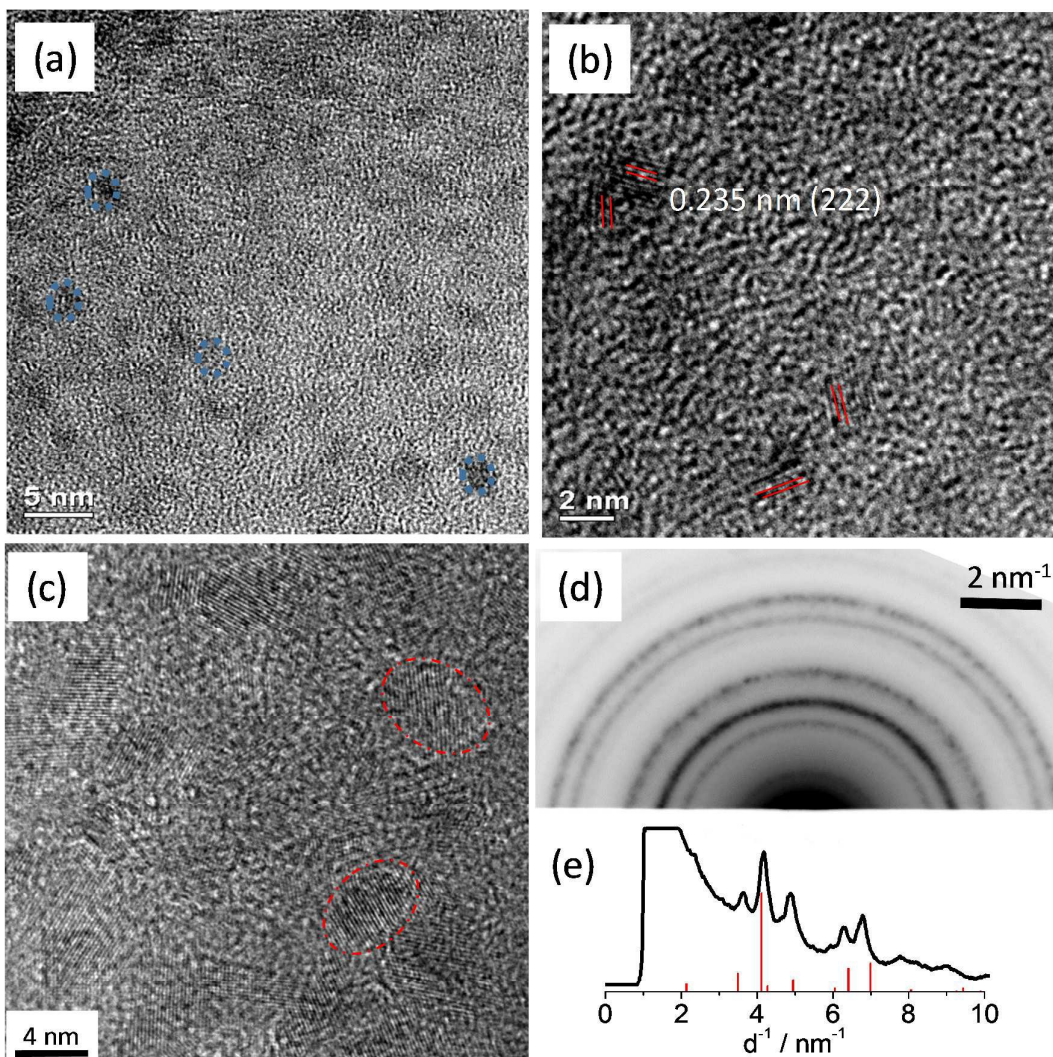

Figure 4 TEM images of the Co_3O_4 nanocrystals from the anodic oxidation of cobalt foil under 4.6 mA (a, b) and 0.7 mA (c). (d) is the SAED pattern of the Co_3O_4 nanocrystals and (e) is a representative linear histogram profile of the SAED pattern starting from the centre of the ring. The powder diffraction file (No. 1-1152) from XRD is shown in vertical lines in (e) for comparison.

We then performed FTIR in order to analyse further the oxide nanocrystals and by-products (Figure 5). As the limiting current for the samples increased from 0.7 mA to 4.6 mA, the relative peak intensity of -COO⁻ against that of Co-O increased

tremendously, suggesting that more acetate related species were produced in the synthesis at higher limiting current. This suggests that the acetate by-products from the oxidation of ethanol is not only detrimental to the relative productivity of Co_3O_4, but effectively inhibits the crystal growth. FTIR analysis (Figure 5) also clearly showed the absorption peak of Co-O, C-O, C=O, C-H and -OH. Below 800 cm^{-1}, the absorption is associated with Co-O stretching and Co-OH bending vibrations.[50] Sharp absorptions at 573 cm^{-1} and 662 cm^{-1} can be attributed to the spinel Co_3O_4[51] as α-Co(OH)$_2$ shows only a broad peak at 634 cm^{-1},[52, 53] which could be obscured by the absorption peak of Co_3O_4. Hydroxyl groups and water are evidenced by the broad bands observed at 3275 cm^{-1} and the broadening of these bands is due to hydrogen bond formation.[54] The FTIR spectrum showed intense bands at 1582 cm^{-1} and 1336 cm^{-1} assigned to asymmetrical stretching v_{as}(-COO$^-$) and symmetrical stretching v_a(-COO$^-$), respectively. The difference between the two bands (v_{as} - v_a ~246 cm^{-1}) is characteristic of unidentate acetate ligands.[55] For the coating calcined at 250 ^{o}C in air, the FTIR (Figure S6) shows intensified peaks for Co-O vibrations and lower intensity -OH peaks, indicating a drastic increase in weight ratio of Co_3O_4 in this final product due to the decomposition of the carboxyl- and hydroxide-containing by-products.
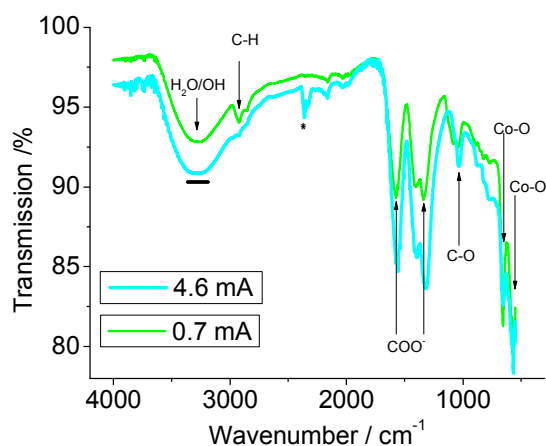

Figure 5 FTIR for powder samples dried at 80 ^{o}C from the solution synthesised at a limiting current of 0.7 mA and 4.6 mA.

In order to analyse further the chemical properties of the powder, XPS was performed before and after calcination at 250 °C, as shown in Figure 6. The C 1s XPS spectrum can be fitted with distinct peaks at around 288.4 eV, 285.4 eV and 284.5 eV, which correspond to the O-C=O, C-OH/C-O-C bond and adventitious carbon, respectively.[56] The peaks corresponding to O-C=O and C-OH/C-O-C decreased dramatically after calcination at 250 °C, implying a decomposition of carboxylate groups upon thermal treatment. The sample dried at 80 °C showed weak peaks at binding energy higher than 405 eV, which can be attributed to nitrates (e.g. NO_3^-, NO_2^- etc), and these disappeared after thermal decomposition. The O 1s spectrum for the sample at 80 °C can be fitted with three peaks centred at 529.9 eV, 531.4 eV and 532.1 eV. The binding energy of oxygen bound to cobalt in Co_3O_4, CoOOH and $Co(OH)_2$ occurs between 529.4 eV and 530.7 eV,[57] so the peak at 529.9 eV can be assigned to Co-O bonding. The peaks at 531.4 eV and 532.1 eV could be ascribed to C-O and absorbed water molecules, respectively.[58]
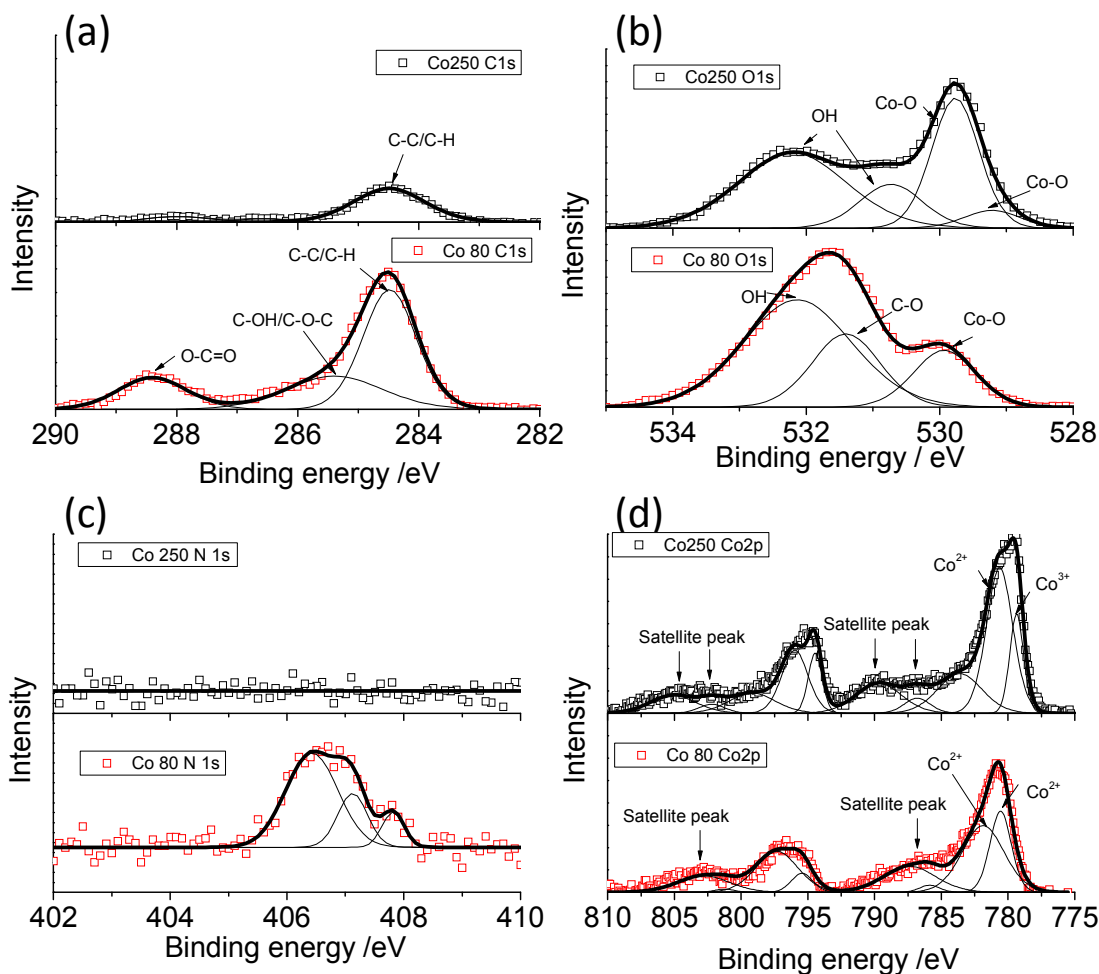
Figure 6 XPS of the coating after calcination at 80 °C (Co 80) and 250 ^{o}C (Co 250): C 1s (a), O 1s (b), N 1s (b) and Co 2p (d). The inset in (a) is the magnified region from 292-286 eV.

Considering that the TEM results show only Co_3O_4 spinels as the crystalline material and FTIR results show -OH and C=O groups, the by-products could be cobalt hydroxide acetate. The Co 2p region of the samples annealed at 80 °C showed one satellite peak at 786.8 eV with respect to the main $2p_{3/2}$ peak (780.51 eV) , which is quite close to divalent cobalt in CoO or $Co(OH)_2$.[59] On the contrary, two satellite peaks (786.8 eV and 789.8 eV), with respect to the main $2p_{3/2}$ peak, revealed that the sample calcined at 250 °C could be a mixture of Co_3O_4, CoO or $Co(OH)_2$. The formation of Co_3O_4 can be also implied from the fitted peak at a lower binding energy

of 779.3 eV which is due to Co^{3+}.[54] Moreover, the evolution of a sharp peak at around 1.0 eV in the valence band XPS (Figure S7) after the calcination at 250 ^{o}C is a clear indication of Co^{3+} accumulation during the calcination process.[60]

The amount of by-product other than the Co_3O_4 crystals was evaluated via TGA (Figure 7) on the sample synthesised at 4.6 mA limiting current. An obvious weight loss of 40.9 % was observed from room temperature to 500 ^{o}C. The first 8.5% could be attributed to the loss of residual ethanol or absorbed moisture. The second weight loss (32.4%), peaked at 225 ^{o}C,[54] is higher than that expected for $CoAc_2$ (~200 °C)[61] and therefore ascribed to layered hydroxide cobalt acetates (~ 220°C). The reduction of the product in Ar containing 5% H_2 (Figure 7(b)) after calcination at 500 °C showed a weight loss of 29.1 wt.%, which is close to the theoretical value for the reduction of Co_3O_4 to metallic Co; this indicates that pure Co_3O_4 oxides can be obtained by low-temperature calcination in air.
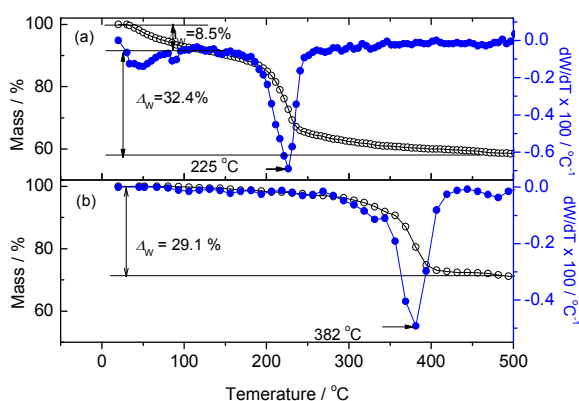

Figure 7 TGA curve in air (a) for the powders collected after the drying of suspension at 80 °C for 1 hour in air and (b) in Ar-5% H_2 after calcination at 500 °C. The right y-ordinates are the derivative of weight against temperature. The derivative of TGA was presented in solid dots.

Characterisation of coating

The coating is a translucent yellowish green colour with a brownish edge as seen in the inset of Figure 8(a). The green tinge could be a result of cobalt (II) hydroxide

intercalated with NO_3^- or CH_3COO^-.[50] It is very difficult to separate the nanoparticles by centrifugation, even at a speed of ten-thousand revolutions per minute (rpm). $Co(OH)_x(Ac)_{2-x}$ layered materials are reported to show a sharp absorption peak at 641 nm,[54] which is not expected to interfere with the absorption of Co_3O_4 nanocrystals near the band edge. UV/Vis absorption spectroscopy (Figure 8(a)) of the dried coating shows an absorption edge around 800 nm and the Tauc plot (Figure 8(b)) shows a bandgap of 1.5 eV which is slightly larger than that for 40 nm diameter Co_3O_4 particles (1.45 eV)[47] as a result of quantum-confinement.
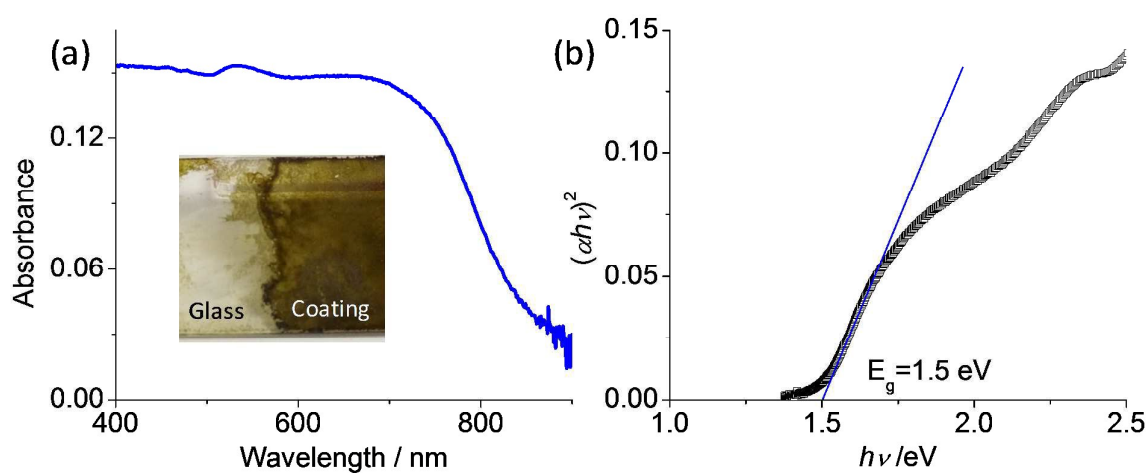

Figure 8 (a) UV/Vis spectroscopy of the coating calcined at 80 $^\circ$C and (b) the corresponding Tauc plot. The inset in (a) is the image of the coating on glass.

Detailed SEM analysis (Figure S8) revealed that a dense coating of 4 μm in thickness with a homogeneous surface can be initially produced; however after calcination at 250 $^\circ$C, heterogeneous particles evolve on the surface due to the decomposition process. Anderson et al.[9] fabricated a solar cell device based on a TiO_2/Co_3O_4 heterojunction using pulsed laser deposition; they observed improvements in efficiency when the Urbach edge, which is due to crystal defects, diminished. A compact and continuous film of nanocrystalline spinel Co_3O_4 with

$Co(OH)_2$ groups on the surface has been reported to be an efficient water splitting catalyst in a Si-based photo-electrochemical cells.[62] Surface defects can also be decreased by sequential deposition of quantum dots and ligands for surface passivation.[63] The 4-μm thick coating dried at 80 ^oC could form a rectified diode with TiO_2 as barrier layer, as shown in Figure S9. The space-charging behaviour could be related to the *p*-type semiconducting behaviour of the system including Co_3O_4 and the by-product[64]. Compared to other methods of synthesising Co_3O_4 spinels (e.g. via thermal decomposition of nitrate, two-electrode electrolysis and hydro-/solvo-thermal synthesis), microplasma-assisted synthesis in ethanol yields a solution that is directly applicable for the formation of a dense coating due to the outstanding dispersion of the particles and organics-containing by-product. Compared to the fabrication of thin films via spin coating of pyrolysable salt of cobalt, the initial content of spinel oxide produced by microplasma decreases the volumetric variation and gaseous release of the reactions leading to a better coating structure.

Discussion

In the initial stages of the microplasma-based process, the cathodic reduction of ethanol is due to trace protons from ionised ethanol, which produce H_2 and leaves basic $CH_3CH_2O^-$ ions in the area near the cathode.[65] The anodic oxidation of metals (e.g. Zr, Mo, Ti and W) in alcohols was actually developed for the production of metal alkoxides along with the production of H_2[66]. H_2 is here expected to be released in air. However it is also possible that molecular hydrogen reacts with ambient air within the plasma leading to H_2O, which will be eventually re-absorbed into ethanol to combine with $CH_3CH_2O^-$ and increase the absolute acidity. The plasma also interacts with ambient air and can promote the reaction between N_2 and oxygen to produce NO_x or ammonia[67] as can also be inferred from the nitrates in our final product and the bond energy of H-H (4.52 eV), which is much lower than that of N≡N (9.8 eV). The

re-absorption of H_2O is insignificant for electrolysis performed with an aqueous electrolyte, but it is extremely important when absolute ethanol is used as the electrolyte. The oxidation of ethanol that involves the cleavage of C-C bonding and the formation of carboxylate can greatly increase the ionic conductivity and contribute to acidify further the solvent in the following reaction period. For the electrolysis with high limiting current, the side reactions that produce acetic acid will dominate and will acidify the solution via the dissolution of NO_x and hydro(per)oxide radicals which will enhance the dissolution of Co_3O_4 nanocrystals.

The difference between the liquid products obtained with the graphite or cobalt anode indicates that cations play an important role. The absence of ^{1}H NMR peaks for HCOOH when cobalt was used as the anode can be attributed to the good catalytic performance of the cobalt containing species for further oxidation of formic acid to carbon dioxide.[68] Du *et al.*[69] studied the plasma reforming of gaseous ethanol and water and found that HCOOH, CH_3COOH and CH_3COCH_3 formed in the liquid phase; reactions at the plasma/ethanol interface were complex, since they involved surface charge accumulation and dispersion through the gas-liquid interface[70]. For the DC glow discharge with the oxidisable cations, the oxidation induced by H_2O_2 produced in aqueous systems is generally considered as an unfavourable reaction[71]; however, in our case, we found that the oxidation process can be beneficial for the production of quantum dots via the oxidation of ethanol to provide anions for the dissolution of cobalt species. As microplasma processing can induce polymerisation, the anodisation of metals in organics can be used for the direct production of composites formed by quantum dots and polymers with improved catalytic performance to water splitting[47].

Conclusions

Crystalline Co_3O_4 quantum dots with mean diameters of 1.9 nm or 4.6 nm were synthesised via a DC plasma in absolute ethanol under an initial applied voltage of 3.0 kV. The study also revealed that when the sacrificial cobalt electrode was replaced with a graphite anode, pure ethanol oxidises to acetate, which in turn undergoes a condensation reaction with ethanol to form esters. The Co-oxide nanocrystals are well-dispersed in the liquid phase and a compact film from the suspension can be deposited on TiO_2 film to make a rectified diode. Ethanol oxidation is enhanced when the DC limiting current is increased, which also decreases the size of the Co_3O_4 quantum dots. By-products were also observed from the dried samples and have been determined to contain carboxylate groups with trace NO_3^- anions according to the XPS and TGA results. With minimum thermal treatment at 250 $^{\circ}$C in air, a film of spinels can be obtained with the conversion of the by-products. The formation of carboxylate groups provides the charge carrier and affects the production of nanocrystalline Co_3O_4. Although the focus was on the synthesis of cobalt nanocrystals, this study also highlights important and more general findings relevant to plasma processing with organic solvents.

Conflicts of interest

There are no conflicts to declare

Acknowledgements

Author Contributions

C.N. prepared sample and performed the characterisation with D.C. (TEM), C.R.(XPS, *j*-V curve), J.H. (TGA,SEM,TEM,XRD), Z.F.(NMR) and D.B.P.(absorption, PL). C.N. analysed the data and initiated the draft which is revised by J.N., D.X., P.M., JTSI and D.M.. All authors commented on the manuscript and the project is overseen by D.M..

Notes and references

1.   L. Al Juhaiman, L. Scoles, D. Kingston, B. Patarachao, D. Wang and F. Bensebaa, *Green Chem.*, 2010, **12**, 1248-1252.
2.   Y. Chang, X. Yao, L. Mi, G. Li, S. Wang, H. Wang, Z. Zhang and Y. Jiang, *Green Chem.*, 2015, **17**, 4439-4445.
3.   N. Shirahata, D. Hirakawa and Y. Sakka, *Green Chem.*, 2010, **12**, 2139-2141.
4.   F. Cheng, J. Shen, B. Peng, Y. Pan, Z. Tao and J. Chen, *Nat Chem*, 2011, **3**, 79-84.
5.   T. He, D. Chen, X. Jiao, Y. Wang and Y. Duan, *Chem. Mater.*, 2005, **17**, 4023-4030.
6.   Q. Jiang, H. Zhang and S. Wang, *Green Chem.*, 2016, **18**, 662-666.
7.   Z.-j. Wang, Y. Zhao, L. Cui, H. Du, P. Yao and C.-j. Liu, *Green Chem.*, 2007, **9**, 554-559.
8.   W. Chu, L.-N. Wang, P. A. Chernavskii and A. Y. Khodakov, *Angewandte Chemie International Edition*, 2008, **47**, 5052-5055.
9.   B. Kupfer, K. Majhi, D. A. Keller, Y. Bouhadana, S. Rühle, H. N. Barad, A. Y. Anderson and A. Zaban, *Adv. Energy Mater.*, 2015, **5**, 1401007.
10. V. K. Patel, J. R. Saurav, K. Gangopadhyay, S. Gangopadhyay and S. Bhattacharya, *RSC Advances*, 2015, **5**, 21471-21479.
11. M. Ebadi, M. A. Mat-Teridi, M. Y. Sulaiman, W. J. Basirun, N. Asim, N. A. Ludin, M. A. Ibrahim and K. Sopian, *RSC Advances*, 2015, **5**, 36820-36827.
12. M. Jing, Y. Yang, Y. Zhu, H. Hou, Z. Wu and X. Ji, *Electrochim. Acta*, 2014, **141**, 234-240.
13. N. Zhang, J. Shi, S. S. Mao and L. Guo, *Chem. Commun. (Cambridge, U. K.)*, 2014, **50**, 2002-2004.
14. D. Walsh, N. M. Sanchez-Ballester, K. Ariga, A. Tanaka and M. Weller, *Green Chem.*, 2015, **17**, 982-990.
15. M. Davide and R. M. Sankaran, *J. Phys. D: Appl. Phys.*, 2010, **43**, 323001.
16. Z. Wang, Y. Lu, H. Yuan, Z. Ren, C. Xu and J. Chen, *Nanoscale*, 2015, **7**, 20743-20748.
17. J. Senthilnathan, C.-C. Weng, J.-D. Liao and M. Yoshimura, *Scientific Reports*, 2013, **3**, 2414.
18. X. Huang, Y. Li and X. Zhong, *Nanoscale Research Letters*, 2014, **9**, 1-7.
19. D. Mariotti, J. Patel, V. Švrček and P. Maguire, *Plasma Processes Polym.*, 2012, **9**, 1074-1085.
20. P. Maguire, D. Rutherford, M. Macias-Montero, C. Mahony, C. Kelsey, M. Tweedie, F. Pérez-Martin, H. McQuaid, D. Diver and D. Mariotti, *Nano Lett.*, 2017, **17**, 1336-1343.
21. R. Buitrago-Sierra, M. J. Garcia-Fernandez, M. M. Pastor-Blas and A. Sepulveda-Escribano, *Green Chem.*, 2013, **15**, 1981-1990.
22. C. Du and M. Xiao, *Scientific Reports*, 2014, **4**, 7339.
23. Y. Lu, Z. Ren, H. Yuan, Z. Wang, B. Yu and J. Chen, *RSC Advances*, 2015, **5**, 62619-62623.
24. T. Velusamy, A. Liguori, M. Macias-Montero, D. B. Padmanaban, D. Carolan, M. Gherardi, V. Colombo, P. Maguire, V. Svrcek and D. Mariotti, *Plasma Processes Polym.*, 2017, DOI: 10.1002/ppap.201600224, 1600224.
25. L. Zhao, Y. Wang, Z. Sun, A. Wang, X. Li, C. Song and Y. Hu, *Green Chem.*, 2014, **16**, 2619-2626.
26. C. Richmonds, M. Witzke, B. Bartling, S. W. Lee, J. Wainright, C.-C. Liu and R. M. Sankaran, *J. Am. Chem. Soc.*, 2011, **133**, 17582-17585.
27. T. Sudare, T. Ueno, A. Watthanaphanit and N. Saito, *The Journal of Physical Chemistry A*, 2015, **119**, 11668-11673.
28. T. Sudare, T. Ueno, A. Watthanaphanit and N. Saito, *Phys. Chem. Chem. Phys.*, 2015, **17**, 30255-30259.
29. B. H. Milosavljevic and O. I. Micic, *The Journal of Physical Chemistry*, 1978, **82**, 1359-1362.

30. V. Svrcek, K. Dohnalova, D. Mariotti, M. T. Trinh, R. Limpens, S. Mitra, T. Gregorkiewicz, K. Matsubara and M. Kondo, *Adv. Funct. Mater.*, 2013, **23**, 6051-6058.

31. N. Y. Kim and P. E. Laibinis, *J. Am. Chem. Soc.*, 1999, **121**, 7162-7163.

32. Y. Li, X. Zhong, A. E. Rider, S. A. Furman and K. Ostrikov, *Green Chem.*, 2014, **16**, 2566-2570.

33. S.-L. Chen, A.-C. Xu, J. Tao, H.-J. Tao, Y.-Z. Shen, L.-M. Zhu, J.-J. Jiang, T. Wang and L. Pan, *Green Chem.*, 2016, **18**, 2793-2801.

34. J. M. Patete, X. Peng, C. Koenigsmann, Y. Xu, B. Karn and S. S. Wong, *Green Chem.*, 2011, **13**, 482-519.

35. B. B. Chen, Z. X. Liu, W. C. Deng, L. Zhan, M. L. Liu and C. Z. Huang, *Green Chem.*, 2016, **18**, 5127-5132.

36. W. M. Nelson, *Green Solvents for Chemistry: Perspectives and Practice*, Oxford University Press, New York, 2003.

37. P. Anastas and N. Eghbali, *Chem. Soc. Rev.*, 2010, **39**, 301-312.

38. A. K. Rath, M. Bernechea, L. Martinez, F. P. G. D. Arquer, J. Osmond and G. Konstantatos, *Nat. Photonics*, 2012, **6**, 529-534.

39. C. McDonald, C. Ni, V. Svrcek, M. Lozac'h, P. A. Connor, P. Maguire, J. T. S. Irvine and D. Mariotti, *Nanoscale*, 2017, **9**, 18759-18771.

40. P. Ballinger and F. A. Long, *J. Am. Chem. Soc.*, 1960, **82**, 795-798.

41. H. E. Gottlieb, V. Kotlyar and A. Nudelman, *The Journal of organic chemistry*, 1997, **62**, 7512-7515.

42. N. Sato and T. Ohtsuka, *J. Electrochem. Soc.*, 1978, **125**, 1735-1740.

43. D. Mariotti, V. Švrček, J. W. J. Hamilton, M. Schmidt and M. Kondo, *Adv. Funct. Mater.*, 2012, **22**, 954-964.

44. M. Long, W. Cai, J. Cai, B. Zhou, X. Chai and Y. Wu, *The Journal of Physical Chemistry B*, 2006, **110**, 20211-20216.

45. M. M. Waegele, H. Q. Doan and T. Cuk, *The Journal of Physical Chemistry C*, 2014, **118**, 3426-3432.

46. L. Qiao, H. Y. Xiao, H. M. Meyer, J. N. Sun, C. M. Rouleau, A. A. Puretzky, D. B. Geohegan, I. N. Ivanov, M. Yoon, W. J. Weber and M. D. Biegalski, *Journal of Materials Chemistry C*, 2013, **1**, 4628-4633.

47. P. Y. Keng, B. Y. Kim, I.-B. Shim, R. Sahoo, P. E. Veneman, N. R. Armstrong, H. Yoo, J. E. Pemberton, M. M. Bull, J. J. Griebel, E. L. Ratcliff, K. G. Nebesny and J. Pyun, *ACS Nano*, 2009, **3**, 3143-3157.

48. Z. Yang, L. Lu, V. F. Berard, Q. He, C. J. Kiely, B. W. Berger and S. McIntosh, *Green Chem.*, 2015, **17**, 3775-3782.

49. N. Zhang, J. Shi, F. Niu, J. Wang and L. Guo, *Phys. Chem. Chem. Phys.*, 2015, **17**, 21397-21400.

50. Z.-A. Hu, Y.-L. Xie, Y.-X. Wang, L.-J. Xie, G.-R. Fu, X.-Q. Jin, Z.-Y. Zhang, Y.-Y. Yang and H.-Y. Wu, *The Journal of Physical Chemistry C*, 2009, **113**, 12502-12508.

51. R. Xu and H. C. Zeng, *Langmuir*, 2004, **20**, 9780-9790.

52. R. Li, Z. Hu, X. Shao, P. Cheng, S. Li, W. Yu, W. Lin and D. Yuan, *Scientific Reports*, 2016, **6**, 18737.

53. X. Ge, C. D. Gu, X. L. Wang and J. P. Tu, *The Journal of Physical Chemistry C*, 2014, **118**, 911-923.

54. L. Poul, N. Jouini and F. Fiévet, *Chem. Mater.*, 2000, **12**, 3123-3132.

55. M. Taibi, S. Ammar, N. Jouini, F. Fievet, P. Molinie and M. Drillon, *J. Mater. Chem.*, 2002, **12**, 3238-3244.

56. I. O. Ucar, M. D. Doganci, C. E. Cansoy, H. Y. Erbil, I. Avramova and S. Suzer, *Appl. Surf. Sci.*, 2011, **257**, 9587-9594.

57. J. Yang, H. Liu, W. N. Martens and R. L. Frost, *The Journal of Physical Chemistry C*, 2009, **114**, 111-119.

58. T. V. Semenistaya, in *Advanced Materials: Manufacturing, Physics, Mechanics and Applications*, eds. A. I. Parinov, S.-H. Chang and Y. V. Topolov, Springer International Publishing, Cham, 2016, DOI: 10.1007/978-3-319-26324-3_5, pp. 61-77.

59. M. C. Biesinger, B. P. Payne, A. P. Grosvenor, L. W. M. Lau, A. R. Gerson and R. S. C. Smart, *Appl. Surf. Sci.*, 2011, **257**, 2717-2730.

60. M. A. Langell, M. D. Anderson, G. A. Carson, L. Peng and S. Smith, *Physical Review B*, 1999, **59**, 4791-4798.

61. R. W. Grimes and A. N. Fitch, *J. Mater. Chem.*, 1991, **1**, 461-468.

62. J. Yang, J. K. Cooper, F. M. Toma, K. A. Walczak, M. Favaro, J. W. Beeman, L. H. Hess, C. Wang, C. Zhu, S. Gul, J. Yano, C. Kisielowski, A. Schwartzberg and I. D. Sharp, *Nat. Mater.*, 2017, **16**, 335-341.

63. J. Tang, K. W. Kemp, S. Hoogland, K. S. Jeong, H. Liu, L. Levina, M. Furukawa, X. Wang, R. Debnath, D. Cha, K. W. Chou, A. Fischer, A. Amassian, J. B. Asbury and E. H. Sargent, *Nat. Mater.*, 2011, **10**, 765-771.

64. Z. a. Tan, W. Zhang, D. Qian, C. Cui, Q. Xu, L. Li, S. Li and Y. Li, *Phys. Chem. Chem. Phys.*, 2012, **14**, 14217-14223.

65. D. C. Bradley, in *Prog. Inorg. Chem.*, John Wiley & Sons, Inc., 2007, DOI: 10.1002/9780470166031.ch7, pp. 303-361.

66. E. Kovsman, S. Andruseva, L. Solovjeva, V. Fedyaev, M. Adamova and T. Rogova, *J. Sol-Gel Sci. Technol.*, 1994, **2**, 61-66.

67. T. Haruyama, T. Namise, N. Shimoshimizu, S. Uemura, Y. Takatsuji, M. Hino, R. Yamasaki, T. Kamachi and M. Kohno, *Green Chem.*, 2016, **18**, 4536-4541.

68. N. Kakati, J. Maiti, S. H. Lee, S. H. Jee, B. Viswanathan and Y. S. Yoon, *Chem. Rev. (Washington, DC, U. S.)*, 2014, **114**, 12397-12429.

69. C. Du, J. Mo, J. Tang, D. Huang, Z. Mo, Q. Wang, S. Ma and Z. Chen, *Appl. Energy*, 2014, **133**, 70-79.

70. W. S. Kang, M. Hur, J. Y. Lee, J.-O. Lee and Y.-H. Song, *Plasma Chem. Plasma Process.*, 2016, **36**, 1021-1029.

71. A. Hickling and M. D. Ingram, *Journal of Electroanalytical Chemistry (1959)*, 1964, **8**, 65-81.

Anoidisation of Co foil in absolute ethanol electrolyte with microplasma cathode produces size-controllable Co_3O_4 quantum dots.